Mechanism of Interaction of the Double-Stranded RNA (dsRNA) Binding Domain of Protein Kinase R with Short dsRNA Sequences†

Jason W. Ucci,‡ Yumiko Kobayashi,‡ Gregory Choi,‡ Andrei T. Alexandrescu,‡ and James L. Cole*,‡,§

Department of Molecular and Cell Biology and National Analytical Ultracentrifugation Facility, University of Connecticut, Storrs, Connecticut 06269-3125

Received July 28, 2006; Revised Manuscript Received October 6, 2006

ABSTRACT: The dsRNA-activated protein kinase (PKR) plays a major role in the cellular response to viral infection. PKR contains an N-terminal dsRNA binding domain (dsRBD) and a C-terminal kinase domain. The dsRBD consists of two tandem copies of a conserved double-stranded RNA binding motif, dsRBM1 and dsRBM2. dsRNA binding is believed to activate PKR by inducing dimerization and subsequent autophosphorylation reactions. We have characterized the function of the dsRBD by assessing the binding of dsRBM1 and dsRBD to a series of dsRNA sequences ranging from 15 to 45 bp. For dsRBM1, the binding stoichiometries agree with an overlapping ligand binding model where the motif binds to multiple faces of the dsRNA duplex and overlaps along the helical axis. Similar behavior is observed for a dsRBD containing both dsRBM1 and dsRBM2 for sequences up to 30 bp; however, the binding affinity is enhanced 30-fold. Longer dsRNA sequences exhibit lower-than-expected stoichiometries, indicating a change in binding mode. NMR spectroscopy was used to define the regions of the dsRBD that interact with dsRNA. dsRNA binding induces exchange broadening of cross-peaks in $^{1}H-^{15}N$ HSQC spectra. For a 20 bp dsRNA, the resonances most affected map to the known dsRNA binding regions of dsRBM1 as well as the N-terminus of dsRBM2. For a longer 40 bp sequence, additional regions of dsRBM2 exhibit enhanced broadening. These data support a model in which dsRBM1 plays the dominant role in binding short dsRNA sequences and dsRBM2 makes additional interactions with the longer sequences capable of activating PKR.

Protein kinase R (PKR) is an interferon-induced kinase activated by dsRNA[1] (*1*). The enzyme is synthesized in a latent state, but upon binding dsRNA, it undergoes autophosphorylation at multiple serine and threonine residues, resulting in activation. PKR is a member of the family of stress-response kinases that also includes GCN2, HRI, and PERK (*2*). These enzymes contain a conserved eIF2α kinase domain linked to different regulatory domains, and they inhibit translation by phosphorylation of eukaryotic initiation factor eIF2α. Production of dsRNA during viral infection thus leads to PKR activation and subsequent inhibition of viral protein synthesis.

In PKR, the regulatory module consists of an N-terminal pair of double-stranded RNA binding motifs (dsRBM), here termed dsRBM1 and dsRBM2 (*3*, *4*). The dsRBM is widely distributed among eukaryotic, prokaryotic, and viral proteins that interact with dsRNA (*5*−*7*). The structures of several dsRBMs have been reported in free (*8*−*13*) and dsRNA-bound forms (*14*−*19*). Each adopts a conserved α*βββ*α fold where the two helices pack on one side of the three-stranded *β* sheet. In the NMR structure of the PKR dsRNA binding domain (dsRBD), the two motifs each adopt the canonical dsRBM fold and are connected by an unstructured linker of ∼20 amino acids (*11*). As exemplified by the crystal structure of Xlrbpa2 bound to dsRNA, the dsRBM contains three dsRNA binding regions that interact with successive minor, major, and minor grooves along one face of the duplex, spanning ∼16 bp (*17*). Structural (*14*−*18*) and biochemical (*20*) data indicate that binding of the dsRBM to duplex RNA is not sequence specific. However, there is evidence for selection of specific RNA secondary structural features (*13*, *21*−*23*).

Despite intensive investigation, the mechanism of activation of PKR by dsRNA is not well understood. An autoinhibition model for PKR in which dsRNA binding activates the enzyme by inducing a conformational change that relieves the latent kinase of the inhibition imparted by the interaction of the kinase with the dsRBD has been proposed (*24*−*27*). Intrinsic tryptophan fluorescence (*28*) and electrophoretic mobility shift measurements (*29*) support a dsRNA-induced conformational change. In the context of a dsRBD construct, NMR resonances from dsRBM2 are broadened or disappear upon addition of an exogenous kinase domain, suggesting that it contacts the catalytic domain (*25*). In contrast, ATP binding and atomic force microscopy data indicate an open

† This work was supported by Grants AI-53615 from the NIH (J.L.C.) and MCB 0236316 from the NSF (A.T.A.).

* To whom correspondence should be addressed: Department of Molecular and Cell Biology, 91 N. Eagleville Rd., U-3125, Storrs, CT 06269-3125. Phone: (860) 486-4333. Fax: (860) 486-4331. E-mail: james.cole@uconn.edu.

‡ Department of Molecular and Cell Biology.

§ National Analytical Ultracentrifugation Facility.

[1] Abbreviations: CD, circular dichroism; dsRBD, dsRNA binding domain; dsRBM, dsRNA binding motif; dsRBM1, dsRNA binding motif 1 consisting of PKR residues 6−79; dsRBM2, dsRNA binding motif 2 consisting of PKR residues 96−169; dsRNA, double-stranded RNA; eIF2α, eukaryotic initiation factor 2α.

10.1021/bi061531o CCC: $37.00
Published on Web 12/09/2006

conformation for the latent enzyme where the kinase active site is fully accessible to substrate (*30*).

Binding to dsRNA is also believed to enhance dimerization of PKR which facilitates intermolecular autophosphorylation. Latent PKR exists in a weak monomer−dimer equilibrium with a K_d of 500 μM (*31*). PKR autophosphorylation induced by dsRNA is second-order with respect to enzyme concentration, which suggests that dimerization is required for activation (*32*). A dimerization model also accounts for the observation that low concentrations of dsRNA activate PKR but higher concentrations are inhibitory (*33*−*35*). Presumably, dilution of PKR monomers onto separate molecules of dsRNA at high activator concentrations prevents productive dimerization. Dimerization of the isolated dsRBD has also been reported (*36*−*39*), and PKR dimerization is believed to be mediated by interactions involving the dsRBD (*37*, *38*, *40*, *41*) and a second dimerization motif lying between residues 244 and 296 (*39*).

The ability of dsRNA to bind PKR and induce autophosphorylation is dependent on length. Gel shift measurements indicate a minimum size of either 16−18 (*20*) or 30 bp (*29*, *42*) is required for binding to heteropolymeric dsRNA. At least 30 bp is need for activation (*29*). Binding stoichiometry analysis indicated a minimal site size for saturation of 11 bp/PKR (*20*, *29*, *42*). We recently examined the interaction of PKR with a 20 bp dsRNA using sedimentation equilibrium and CD (*43*). These solution methods indicated a higher binding stoichiometry of three dsRBDs/20 bp RNA. This stoichiometry implies a small site size of 6−7 bp that is not compatible with structures of dsRBM−RNA complexes. This discrepancy led us to propose an overlapping ligand binding model in which binding occurs on multiple faces of the dsRNA duplex, and dsRBD molecules overlap along the helical axis (*43*).

Although some perturbations of the standard Watson−Crick base pairing block the ability of dsRNA to activate PKR, others do not, and the detailed structural requirements for binding and activation of PKR remain unclear. Homopolymeric dsRNA such as poly(I)·poly(C) is a potent activator of PKR; however, random incorporation of guanosine bases into the poly(C) strand to produce I·G mismatches blocks activation in a dose-dependent manner (*44*). PKR is activated by heteropolymeric dsRNAs containing tandem A·G mismatches (*45*). Some highly structured viral RNAs, such as adenovirus type 2 VAI (*46*), bind to PKR but fail to activate the kinase and thus act as in vivo inhibitors of PKR activation by dsRNA. In contrast, the HIV-1 TAR stem−loop motif contains only 24 bp of RNA duplex interrupted by three bulges but does stimulate PKR, albeit 5−6-fold less potently than poly(I)·poly(C) (*47*). Affinity cleavage data demonstrate that RNAs that activate PKR, such as TAR, bind both dsRBMs, whereas RNAs that fail to activate, such as VAI, bind only to dsRBM1 (*48*).

To provide a foundation for understanding the mechanism of PKR interactions with the wide range of complex, naturally occurring RNA activators and inhibitors, it is first necessary to define the interactions with simple, homogeneous dsRNA sequences. Here, we have extended our initial studies of binding of a dsRBD to a single 20 bp dsRNA to encompass sequences ranging from the minimal length dsRNA capable of binding PKR to dsRNAs capable of eliciting strong activation of autophosphorylation. The contribution of the second motif to dsRNA binding was assessed by comparing dsRBD with a construct containing only dsRBM1. We find that the binding stoichiometries for dsRBM1 obey the overlapping lattice model. Similar behavior is observed for the dsRBD construct containing both dsRNA binding motifs for sequences of up to 35 bp. With longer dsRNAs, however, smaller stoichiometries are observed, indicating a change in binding mode. RNA binding leads to differential broadening of NMR signals from the dsRBD. The resonances with the strongest ligand concentration dependence map to the consensus dsRNA-binding site. When a 20 bp dsRNA is titrated into dsRBD, dsRBM1 has stronger concentration dependence than dsRBM2. With a 40 bp dsRNA, the sensitivity of the two motifs is more comparable. Our results support a model in which dsRBM1 has a dominant role in molecular recognition of short dsRNA sequences, whereas both motifs participate significantly in binding to longer dsRNA sequences.

Chart 1

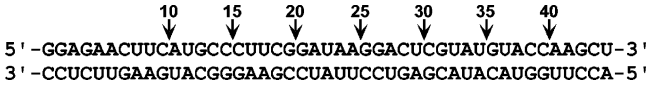

MATERIALS AND METHODS

Reagents and Materials. dsRBD (PKR residues 1−184) was expressed and purified as previously reported (*43*). The gene for dsRBM1 (PKR residues 1−91) was cloned into pET-11a. This plasmid was transformed into BL21(DE3) *Escherichia coli* expression cells (Novagen, Rosetta pLysS). Cells were grown at 37 °C in LB medium containing 50 μg/mL carbenicillin and 34 μg/mL chloramphenicol. For NMR samples, cells were grown in M9 minimal medium supplemented with carbenicillin, chloramphenicol, and 1 g/L [^{15}N]ammonium chloride. Expression was induced at an OD_{600} of 0.6 by the addition of 1 mM isopropyl 1-thio-β-D-galactopyranoside. Cells were grown for an additional 3 h at 37 °C and were harvested by centrifugation at 3000*g* for 15 min. The pellets were resuspended in buffer A [20 mM Bicine, 50 mM NaCl, 1 mM EDTA, 5% glycerol, and 10 mM β-mercaptoethanol (pH 8.65)] containing a protease inhibitor cocktail (Sigma). Cell lysis was accomplished by sonication (Fisher sonic dismembrator) for 10 min. After addition of 2% (w/v) polyethyleneimine, the lysate was incubated on ice for 15 min and the supernatant was collected by centrifugation at 30000*g* for 15 min. The supernatant was loaded onto an S-Sepharose FF (Amersham) column, and dsRBM1 was eluted with a NaCl gradient. Fractions containing dsRBM1 were pooled, diluted 3:1 with buffer A containing no NaCl, and loaded onto heparin Sepharose FF. The column was eluted with a NaCl gradient, and fractions containing pure dsRBM1 were pooled, concentrated, and stored at −80 °C. The dsRBM1 concentration was measured by absorbance at 280 nm using an ϵ_{280} of 2.98×10^3 M^{-1} cm^{-1}.

Synthetic oligoribonucleotides were purchased from Dharmacon, Inc., deprotected according to the manufacturer's protocol, and purified by denaturing polyacrylamide gel electrophoresis. Complementary oligoribonucleotides were annealed at 60 °C and slowly cooled to room temperature. The sequences (Chart 1) are designed to generate a truncation series in 5 bp increments ranging from 10 to 45 bp.

Analytical Ultracentrifugation. Sedimentation equilibrium analysis of protein−dsRNA interactions was performed using absorption optics with a Beckman-Coulter XL-I analytical ultracentrifuge as previously described (*43*). Unless otherwise indicated, protein and dsRNA samples were buffer exchanged into 20 mM HEPES, 75 mM NaCl, and 0.1 mM EDTA (pH 7.5) using Biogel P6 spin columns (Bio-Rad). Analysis of protein:dsRNA stoichiometry was performed using short (1.3 mm) columns with a sample volume of 55 μL with 10 μL of FC43 and a reference channel of 70 μL of buffer. Experiments were conducted at moderate rotor speeds so that the radial dependence of the solution composition was weak, and the data could be parametrized in terms of an average molecular weight (*49*). The data were collected at 260 nm, where the absorbance of the dsRNA predominates over that of the protein, and the buoyant signal-average molecular weight at this wavelength (M^*_{260}) was obtained by fitting the absorbance gradients to the following expression:

$$A(r,260) = \delta_{260} + A_{0,260} \exp[M^*_{260}\Phi(r^2 - r_0^2)] \quad (1)$$

where $A(r,260)$ is the radial-dependent absorbance at 260 nm, $A_{0,260}$ is the absorbance at arbitrary reference distance r_0, and

$$\Phi = \frac{\omega^2}{2RT} \quad (2)$$

where ω is the angular velocity of the rotor in radians per second, R is the molar gas constant, and T is the absolute temperature. Titrations were performed using a fixed RNA concentration (generally 0.5 μM) and variable protein concentrations. M^*_{260} was plotted as a function of [protein]/[dsRNA], and the average value in the plateau was calculated to give $M^*_{260,\text{plateau}}$. Under conditions were the dsRNA absorbance predominates over that of the protein, the binding stoichiometry, S, is given by

$$S = \frac{M^*_{260,\text{plateau}} - M^*_R}{M^*_P} \quad (3)$$

where M^*_P and M^*_R are the buoyant molecular weights of the pure protein and RNA, respectively. Analyses of protein self-association and protein−dsRNA binding constants were performed using 2.5 mm columns with sample volumes of 108 μL with 10 μL of FC43 and a 123 μL reference channel. Data were collected using absorption optics, and the approach to equilibrium was monitored using the HeteroAnalysis software package (*50*). For analysis of dsRBM1 and dsRBD association states, the data were globally analyzed using a single-ideal species model with HeteroAnalysis. For analyses of protein−dsRNA binding constants, the multiwavelength data sets were globally fit to heteroassociation models as previously described (*43*).

Sedimentation velocity analyses were performed using two-channel charcoal-Epon cells in an An60-Ti rotor at 20 °C and 55 000 rpm with sample and reference volumes of 420 μL. Radial scans were collected using the interference optics at 1 min intervals. The data were initially examined using the *c*(*s*) method with Sedfit to produce a sedimentation coefficient distribution function (*51*). Molecular weights were determined from the sedimentation coefficients and diffusion constants obtained by fitting the data to discrete models of one or more noninteracting species using Sedfit (*52*).

Circular Dichroism Spectroscopy. CD measurements of protein−dsRNA binding stoichiometries were performed using a Jasco J-175 spectrometer with 2 mm path length cuvettes at 20 °C. Small aliquots of concentrated (600 μM) protein were titrated into samples of dsRNA at a concentration of 5 μM, and the increase in ellipticity was measured at 260 nm. The data were corrected for dilution, which did not exceed 10% throughout the titration. The CD titrations were fit to the following expression for stoichiometric binding to obtain S:

$$I = I_0 + \frac{1}{2}\Delta I\left(1 + \frac{[P]}{[R]S} - \left|1 - \frac{[P]}{[R]S}\right|\right) \quad (4)$$

where I is the ellipticity at 260 nm, I_0 is the ellipticity in the absence of bound protein, ΔI is the limiting increase at saturation, [P] is the protein concentration, and [R] is the RNA concentration.

Binding stoichiometry data were interpreted using a model of a large ligand binding to a finite one-dimensional lattice with a ligand site size of N and a lattice length of M (*53*−*55*). The number of ligands bound at saturation (binding stoichiometry, S) is given by the largest integer less than or equal to M/N, and the number of microscopic configurations that have x bound ligands is given by

$$C_x = \frac{(M - Nx + x)!}{(M - Nx)!x!} \quad (5)$$

In the context of an overlapping ligand model (*43*), where adjacent ligands may overlap along the lattice with a minimum offset of Δ, the binding stoichiometry is given by the largest integer that satisfies the following inequality

$$S \leq \frac{M - N}{\Delta} + 1 \quad (6)$$

and the number of configurations is given by

$$C_x = \frac{[M - N - (x - 1)\Delta + x]!}{[M - N - (x - 1)\Delta]!x!} \quad (7)$$

NMR Spectroscopy. NMR experiments were performed at 25 °C using a Varian Inova 600 MHz spectrometer equipped with a cryogenic probe. Samples were prepared in a degassed 90% H_2O/10% D_2O mixture containing 100 μM protein, 100 mM NaCl, and 20 mM sodium phosphate (pH 6.5). To monitor binding, dsRNA concentrations were varied from 0 to 100 μM for the 20-mer and from 0 to 20 μM for the 40-mer. Separate samples were prepared for each titration point to ensure the accuracy of protein and dsRNA concentrations. Binding of dsRNA was characterized by the loss of protein $^1H-^{15}N$ HSQC signals as a function of the concentration of unlabeled nucleic acid. Peak volumes and peak intensities (measured with Felix 2004) gave very similar results, but we elected to use peak intensities since these are more accurately measured and more sensitive to increases in line widths. $^1H-^{15}N$ HQSC experiments were conducted with spectral widths of 8000 × 1850 Hz and digitized into 4096 × 256 complex points for ^1H × ^{15}N dimensions. NMR assignments for dsRBD (*56*) were obtained from the BioM-

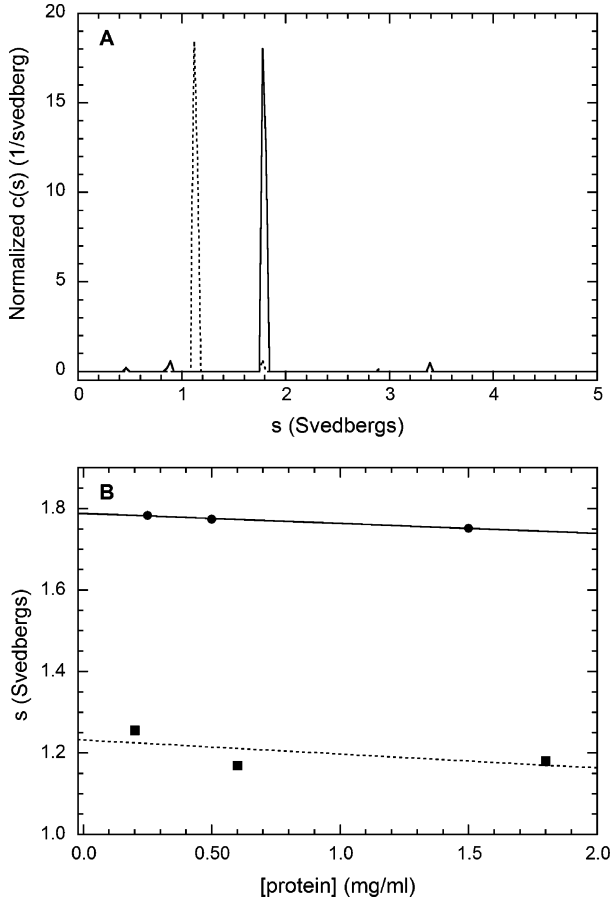

FIGURE 1: Sedimentation velocity analysis of PKR dsRNA binding domain constructs. (A) Continuous sedimentation coefficient distribution analysis of the dsRBD (—) and dsRBM1 (- - -) Conditions: sample concentration, 0.5 mg/mL dsRBD and 0.6 mg/mL dsRBM1; rotor speed, 50 000 rpm; temperature, 20 °C; interference optics. The *c*(*s*) distributions were calculated without regularization and were normalized by loading concentration. (B) Concentration dependence of sedimentation coefficients: dsRBD (●) and dsRBM1 (■). Sedimentation coefficients of the predominant species were obtained by fitting the data to a discrete noninteracting species model using Sedfit.

agResBank (accession number BMRB4110). The $^{1}H-^{15}N$ HSQC correlations of dsRBM1 are nearly identical to those from the corresponding region of dsRBD, so the published assignments for dsRBD were applied to dsRBM1. To analyze the responses of different sites in the protein to dsRNA concentration, we fitted backbone amide $^{1}H-^{15}N$ peak intensities for each residue to the empirical exponential decay function $y = Ie^{-k[RNA]} + C$, where k is an empirical decay constant and C is the baseline intensity at saturating RNA concentrations.

RESULTS

Analysis of Self-Association and Hetero-Association of dsRBD and dsRBM1. Sedimentation velocity and sedimentation equilibrium measurements were used to define the association state of the dsRBD and the isolated dsRBM1. A single major peak is observed near $s = 1.8$ S in a continuous sedimentation coefficient distribution analysis of the dsRBD, indicating that this protein exists as a single homogeneous species (Figure 1A). The sedimentation coefficients decrease slightly with increasing protein concentration due to slight hydrodynamic nonideality; however, there is no evidence for concentration-dependent self-association (Figure 1B). Using the Svedberg equation, we estimate a molecular mass of 21 700 Da, which agrees with the predicted molar mass of 20 262 Da for the monomer. Extrapolation of the sedimentation coefficients to zero protein concentration and correction to standard conditions gives an $s^{\circ}_{20,w}$ of 1.79 S. The frictional ratio, f/f_0, was calculated to be 1.43, indicating that this protein is somewhat asymmetric in solution. dsRBD was also analyzed by sedimentation equilibrium over a concentration range from 0.02 to 0.6 mg/mL. Analysis of individual data channels showed no evidence of concentration-dependent self-association. In a global analysis of data collected at six concentrations and three rotor speeds, a good fit was obtained with a single-ideal species model with a best-fit molecular weight of 19 124 (18 633−19 592) and an rmsd of 0.00342. No improvement in the fit quality was observed using models incorporating self-association or nonideality. Thus, sedimentation velocity and equilibrium measurements indicate that dsRBD is monomeric. We also examined a variety of solvent additives to determine whether they promote association of dsRBD. The dsRBD remained monomeric in sedimentation equilibrium experiments where the NaCl concentration was increased up to 300 mM, where 75 mM NaCl was replaced with 300 mM $NaSO_4$ or upon addition of 5 mM $MgCl_2$ or 20% glycerol.

Sedimentation velocity measurements were also used to define the association state of dsRBM1. As observed for the dsRBD, only one predominant $s = 1.1$ S peak is observed in the *c*(*s*) distribution (Figure 1A). The protein also exhibits a slight decrease in sedimentation coefficient with an increase in concentration, indicative of hydrodynamic nonideality, and also appears to have a slightly asymmetric shape a with frictional ratio of 1.30. From these data, we calculate an $s^{\circ}_{20,w}$ of 1.23 S with a best-fit molecular mass of 10 430 Da (predicted monomer mass of 10 253 Da). Thus, dsRBM1 also does not self-associate under the conditions we examined.

Finally, we investigated the possibility of heterointeractions among dsRBM1, dsRBD, and full-length PKR by sedimentation velocity. Analysis of an equimolar mixture of 20 μM dsRBM1 and dsRBD reveals two predominant peaks at 1.27 and 1.83 S, corresponding to each of the monomeric species. Assuming a shape similar to that of the isolated constructs, a complex of dsRBM1 and dsRBD would be expected to have a sedimentation coefficient of ~2.3 S; however, no feature is observed in this region of the *c*(*s*) distribution, and we do not observe higher *s* peaks that would correspond to higher-order complexes (data not shown). Similarly, analysis of 1:1 mixtures of either dsRBD or dsRBM1 with 8 μM full-length PKR reveals no additional higher features consistent with complex formation. Thus, dsRBM1 and dsRBD do not interact, nor do they bind to full-length PKR under the conditions we have employed.

Binding of dsRBD to dsRNA. We have previously measured the stoichiometry and affinity for binding of dsRBD to a 20 bp dsRNA and interpreted these data in the context of an overlapping ligand model where PKR binds to multiple faces of the dsRNA duplex and overlaps along the helical axis (*43*). Here, we extend these measurements to encompass a series of dsRNAs which span the size range from the minimal dsRNA capable of binding PKR to the minimal length capable of eliciting strong activation of autophosphorylation. Binding stoichiometries were independently mea-

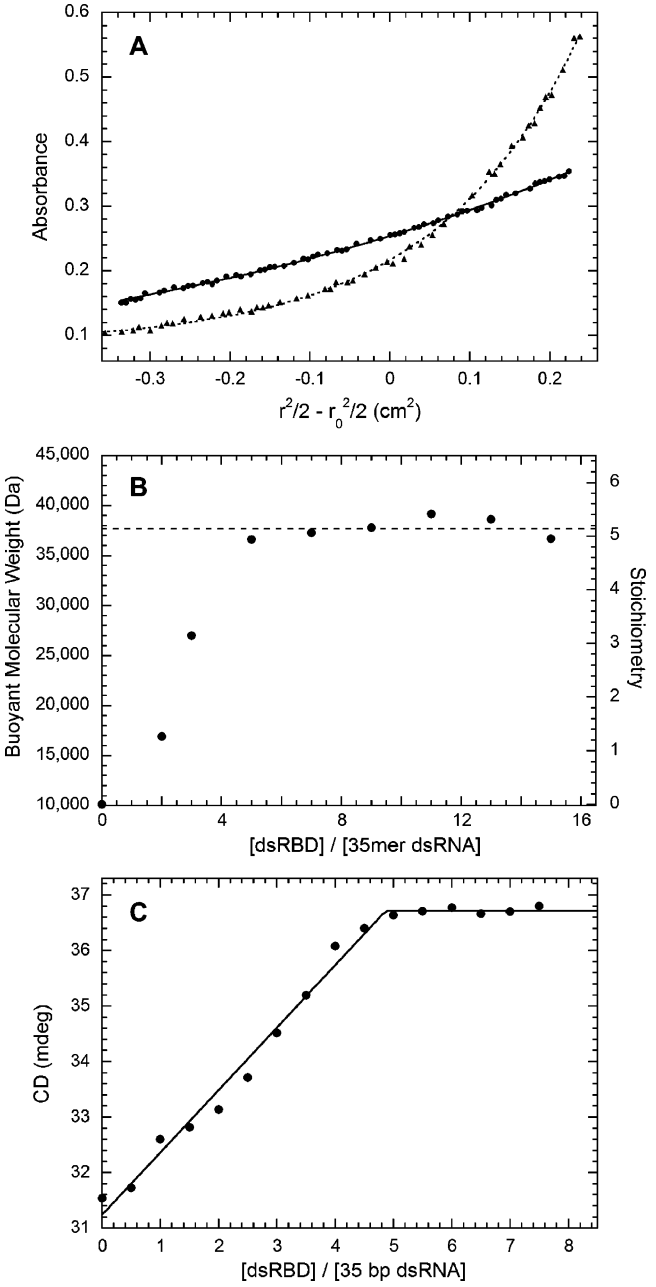

FIGURE 2: Stoichiometry for binding of dsRBD to a 35 bp dsRNA. (A) Sedimentation equilibrium concentration gradients. The data are represented as points, and the fit to a single ideal species model is represented as a solid line: (●) 35 bp dsRNA alone (0.5 μM) and (▲) dsRNA (0.5 μM) with 9 equiv of dsRBD. Conditions: rotor speed, 18 000 rpm; temperature, 20 °C; wavelength, 260 nm. The data were analyzed using heteroanalysis to give buoyant molecular masses of 10 111 and 37 767 Da for the samples containing 0 and 9 equiv of dsRBD, respectively. (B) Sedimentation equilibrium titration. The buoyant molecular masses of the 35 bp dsRNA are plotted as a function of [dsRBD]/[dsRNA]. The average of the data within the plateau region provides a binding stoichiometry of 5.14 dsRBDs/RNA. (C) CD titration. The CD intensity was monitored at 260 nm for a titration of the 35 bp dsRNA with the dsRBD. The dsRNA concentration was 7 μM. The CD data fit to a binding stoichiometry of 4.87 dsRBDs/RNA.

sured by sedimentation equilibrium and CD spectroscopy. Figure 2A shows that addition of an excess of dsRBD to a 35 bp dsRNA results in a sedimentation equilibrium concentration gradient at 260 nm steeper than that for the nucleic acid alone due to the increase in the buoyant signal-average molecular weight (M^*_{260}) associated with binding of protein

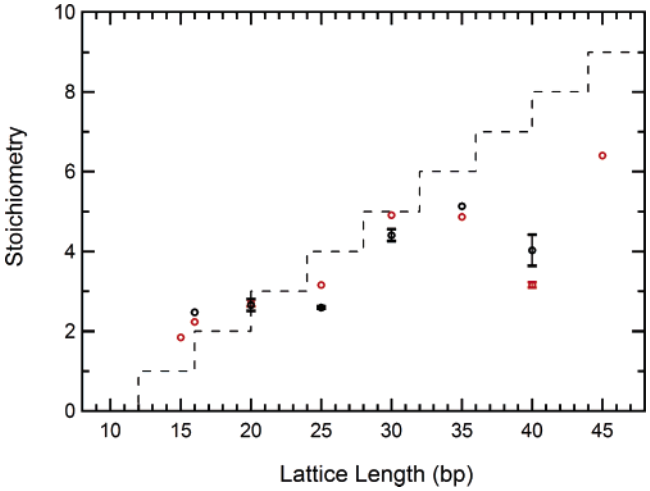

FIGURE 3: Dependence of dsRBD binding stoichiometry on dsRNA length. Stoichiometries were measured by sedimentation equilibrium (black symbols) and CD spectroscopy (red symbols). Errors bars indicate standard deviations from replicate experiments. The dashed line represents the prediction from the overlapping ligand model where $N = 12$ and $\Delta = 4$.

to the RNA. The increase in M^*_{260} plateaus upon saturation of the dsRNA with protein; in this case, the average M^*_{260} in the plateau region corresponds to binding of approximately five dsRBDs to the 35 bp sequence. The binding stoichiometries were verified using CD spectroscopy. In double-stranded nucleic acids, the CD intensity near 260 nm is inversely correlated with the helical winding angle (*57*). The structure of Xlrbpa2 bound to dsRNA indicates that binding of the dsRBM relaxes the winding of dsRNA (*17*), which should result in enhanced CD intensity. Figure 2C shows that binding of the dsRBD to the 35 bp sequence induces an increase in ellipticity at 260 nm consistent with a decrease in the helical winding angle. Under stoichiometric binding conditions, where [dsRNA] $\gg K_d$, these data can be fit to obtain a binding stoichiometry of 4.87 dsRBD/35 bp RNA, thus confirming the sedimentation data.

In Figure 3, the stoichiometries obtained by sedimentation equilibrium and CD measurements are plotted as a function of lattice length. As expected, the stoichiometries increase with lattice length over the range from 15 to 35 bp. Contrary to expectations, the stoichiometry actually decreases at 40 bp. In the context of a simple one-dimensional finite lattice model, S is the highest integer less than or equal to M/N, which implies site sizes of approximately 7−8 bp (e.g., 16/2 for the 16-mer and 30/4 for the 30-mer). This small site size is incompatible with structural data indicating that each dsRBM interacts with ~16 bp. This discrepancy is resolved by considering overlap between adjacent bound ligands, and Figure 3 also shows predictions from the overlapping lattice model for a site size N of 12 bp and a minimal overlap Δ of 4 bp that we previously proposed on the basis of studies of the 20 bp sequence (*43*). The model agrees well with the experimental data over the range of 15−30 bp, but given this small range of RNA sizes, other combinations of N and Δ are also consistent with the data. It is interesting to note that the dsRBD data conform to this model despite the presence of two dsRBMs in this construct.

Remarkably, the binding stoichiometries actually decrease from 35 to 40 bp and then increase again at 45 bp. This effect is not predicted by the model and is observed for both

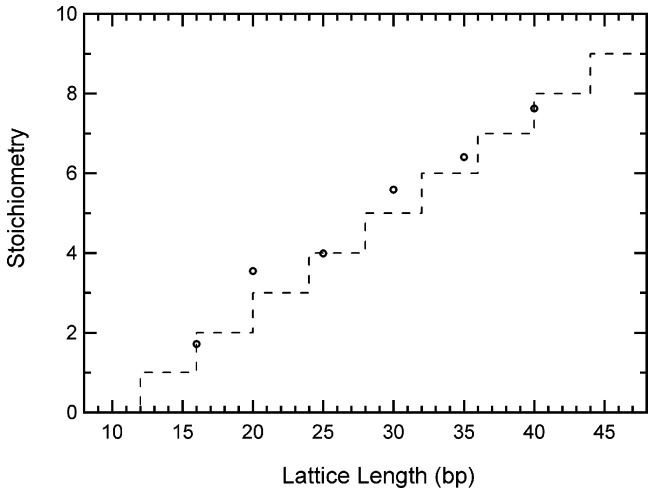

FIGURE 4: Dependence of dsRBM1 binding stoichiometry on dsRNA length. Stoichiometries were measured by sedimentation equilibrium, and the dashed line represents the prediction from the overlapping ligand model where $N = 12$ and $\Delta = 4$.

the sedimentation and CD measurements, which agree to within ±1 dsRBD/RNA. As expected for nonspecific recognition by the dsRNA binding motif (*14*−*18*, *20*), the stoichiometry is not dependent on sequence; dsRBD binds to an unrelated 40 bp sequence with a stoichiometry of 3.75 ± 0.42 (data not shown).

Binding of dsRBM1 to the dsRNA. We examined the RNA binding properties of a construct containing only dsRBM1 to define the contribution of the second motif to the binding stoichiometries. It is known that dsRBM1 binds to dsRNA less strongly than the entire dsRBD (*38*), and this reduced affinity makes it difficult to measure saturation binding stoichiometry under the conditions we have previously used for dsRBD. Although dsRBM1 contains most of the consensus sequence elements of the dsRBM, it lacks a conserved glutamate residue in helix 1 that interacts with the minor groove of dsRNA (*17*). We attempted to enhance the binding affinity by introducing a T16E mutation into dsRBM1; however, the dsRNA interactions were not significantly changed (data not shown). In contrast, reducing the NaCl concentration from 75 to 10 mM sufficiently enhanced the binding affinity to allow us to measure saturation binding stoichiometries.

Figure 4 shows a plot of the saturation binding stoichiometry for dsRBM1 obtained from sedimentation equilibrium analysis as a function of dsRNA length. In contrast to dsRBD, the binding stoichiometries for dsRBM1 increase monotonically with the size of the dsRNA over the entire range that is examined. Over the limited range of 15−30 bp, the data for two constructs are similar; however, for most of the sequences, the binding stoichiometry for dsRBM1 is higher by ∼1 equiv. Thus, for the shorter sequences, the presence of the second motif in dsRBD does not strongly affect the binding site size. Figure 4 also shows that the data agree well with the overlapping model predictions for which $N = 12$ bp and $\Delta = 4$ bp. On the basis of the rms difference between the data and model predictions, approximately equally good fits are obtained when $N = 10-12$ bp and $\Delta = 4$ bp.

Comparison of dsRBM1 and dsRBD Binding Affinities. Having established the binding stoichiometries for the dsRBD and dsRBM1, we measured the affinity for interaction of dsRBM1 with a 20 bp dsRNA by multiwavelength sedimentation equilibrium. These experiments were performed at 75 mM NaCl to facilitate comparison with our previous measurements of dsRBD affinity (*43*). The data were collected at several loading concentrations and three detection wavelengths. The resulting 16 data channels were globally analyzed to determine the binding constants (Figure 5). At the higher salt concentration used in this experiment, it is not possible to saturate the RNA and only two dsRBM1 molecules bind to the 20 bp over the concentration range we employed. Thus, the data were fit to a two-step sequential binding scheme.

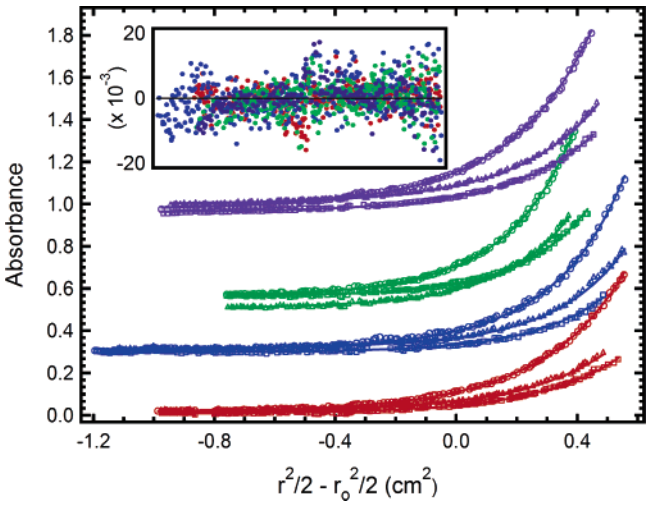

FIGURE 5: Multiwavelength sedimentation equilibrium of dsRBM1 binding to a 20 bp dsRNA. Conditions: rotor speed, 32 000 rpm; temperature, 20 °C; buffer, 75 mM NaCl, 20 mM HEPES, and 0.1 mM EDTA (pH 7.5). Sample concentrations are 0.5 μM RNA and 1.5 μM protein (red), 0.5 μM RNA and 2 μM protein (blue), 0.5 μM RNA and 3 μM protein (green), and 1 μM RNA and 2 μM protein (purple). Detection wavelengths are 230 (triangles), 260 (circles), and 280 nm (squares). Solid lines are a global fit of the data to an overlapping ligand binding model where $N = 12$ and $\Delta = 4$, and the inset shows the residuals. The best fit parameters are as follows: $K_d = 2.38$ [0.93, 4.20] μM with an rmsd of 0.00520. Traces have been vertically offset for clarity.

$$R + P \overset{K_1}{\longleftrightarrow} RP + P \overset{K_2}{\longleftrightarrow} RP_2$$

Using eq 7 for the overlapping lattice model for which $N = 12$ bp and $\Delta = 4$ bp, the stepwise macroscopic binding constants K_1 and K_2 can be expressed in terms of the intrinsic binding constant k where $K_1 = 9k$ and $K_2 = {}^5/_3k$. The sedimentation equilibrium data fit well to this model as indicated by the absence of systematic deviations in the residuals (Figure 5) and an rms deviation of 0.00520. The best fit value of the intrinsic binding constant (k) is 4.21 [2.38, 10.77] × 10^5 M^{-1}. The intrinsic binding constant measured for dsRBD binding under the same conditions is 1.21 × 10^7 M^{-1} (*43*). Thus, although the dsRNA binding stoichiometries are similar for these constructs for shorter dsRNA sequences, the presence of the second motif in dsRBD enhances binding affinity by ∼30-fold relative to dsRBM1 alone.

RNA Binding Monitored by NMR Spectroscopy. NMR spectroscopy was used to define the regions of dsRBD that interact with dsRNA. We characterized dsRBD binding to a

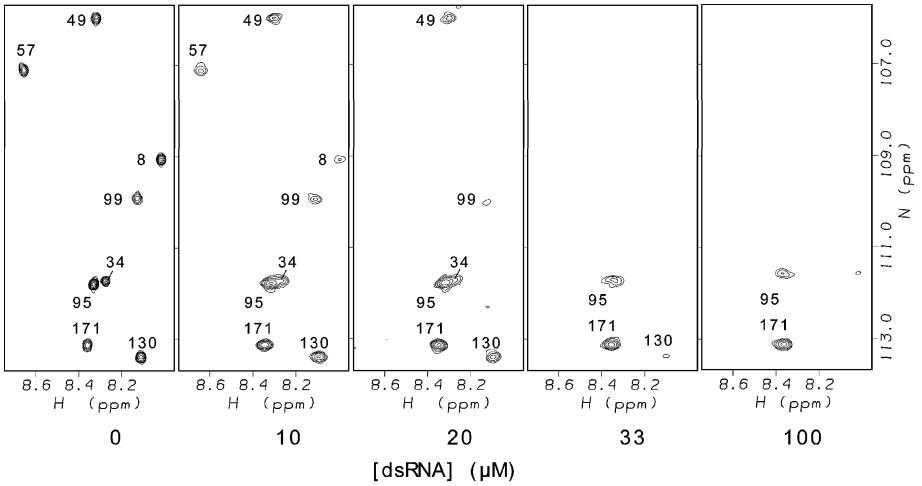

FIGURE 6: Binding of 20-mer dsRNA to the dsRBD monitored by NMR. Representative regions from two-dimensional $^{1}H-^{15}N$ HSQC spectra of 100 μM dsRBD showing the differential broadening of main chain $^{1}H-^{15}N$ correlations with increasing concentrations of dsRNA. Cross-peaks are labeled according to residue position in the dsRBD sequence.

short (20 bp), nonactivating sequence and a longer (40 bp), activating sequence where the binding stoichiometry deviates from the overlapping lattice predictions. Figure 6 shows a portion of the $^{1}H-^{15}N$ HSQC spectrum of dsRBD upon titration with the 20 bp dsRNA. Several resonances undergo decreases in intensity with an increase in dsRNA concentration, whereas others are essentially unperturbed even at the highest RNA concentrations. This behavior is consistent with binding reactions in which interconversion between the RNA-bound and free forms of the protein occurs in the intermediate NMR exchange regime (approximately micromolar dissociation constants). At saturating RNA concentrations (100 μM), only a subset of 15−20 cross-peaks from the dsRBD construct are visible in $^{1}H-^{15}N$ HSQC spectra. These signals are from the linker between the dsRBMs and from the C-terminus of the molecule (not shown). The loss of most peaks at high dsRNA concentrations is probably due to the large mass of the complex formed between the dsRBD and dsRNA (72 kDa). As the concentration of dsRNA increases, the averaged T_2's of the exchanging protein will be predominantly weighted by the T_2's of the bound state, which becomes the predominant form of the protein at saturating dsRNA concentrations. At lower dsRNA concentrations, the differential line broadening of different sites is consistent with intermediate exchange between the bound and free forms of the protein.

In contrast with the dsRNA molecules used in these studies, viral activators and inhibitors with significant secondary structure form complexes with dsRBD that are in slow exchange on the NMR time scale (*13*, *58*). Presumably, the extensive secondary structure in these dsRNAs precludes multiple binding sites, resulting in a 1:1 binding stoichiometry and a unique binding mode compared to the multiple binding events detected with homogeneous dsRNA sequences. Interestingly, the NMR mapping of binding regions on the protein for these studies of homogeneous dsRNA sequences agrees well with the chemical shift mapping results obtained using structured viral RNAs (*13*, *58*).

Structural Mapping of the RNA Binding Sites on dsRBD. To analyze the responses of different sites in the protein to dsRNA concentration, we fitted backbone amide $^{1}H-^{15}N$ peak intensities for each residue to the empirical exponential decay function $y = Ie^{-k[RNA]} + C$, where k is an empirical decay constant and C is the baseline intensity at saturating RNA concentrations. The decay constants for individual residues obtained from this analysis of binding of the dsRBD to the 20 bp dsRNA are summarized in panels A and B of Figure 7. Overall, resonances from dsRBM1 decay faster with increasing RNA concentrations than those from dsRBM2. A notable exception is the N-terminal α helix of dsRBM2, which shows decay constants as large as those from motif 1. ^{15}N relaxation studies of dsRBD in the absence of RNA indicate that the two dsRBMs exist as independent structural units connected by an unstructured linker (*25*). In the RNA-bound state, resonances from residues 94−100 in the linker persist in $^{1}H-^{15}N$ HSQC spectra at the highest RNA concentrations that were studied (Figure 7A). The flexibility of this segment indicates that the potential for the domains to reorient relative to each other still exists in the dsRNA-bound state. The other residues in the linker region between positions 85 and 105, however, are strongly affected by dsRNA binding, indicating that, except for the aforementioned six residues, most of the linker region is no longer flexible in the complex.

We have also characterized binding of isolated dsRBM1 to the same 20 bp RNA. The $^{1}H-^{15}N$ HSQC correlations of the 10 kDa dsRBM1 construct are virtually superimposable on the correlations of the motif 1 segment of the 20 kDa dsRBD construct (not shown), confirming earlier results that showed the structural independence of the dsRBM1 and dsRBM2 motifs in the absence of dsRNA (*11*). As with dsRBD, we observe differential broadening of residues from dsRBM1 upon binding of RNA. Figure 8A shows a structural mapping of the decay constants for dsRBM1. The residues with the largest decay constants (red) primarily map to the first α helix, the loop between strands β1 and β2, and the segments between the end of strand β3 and the beginning of helix α2. These segments correspond to the known RNA binding regions of PKR (*13*, *20*, *23*, *58*) and of related dsRBMs (*14*, *17*, *18*). Thus, the observed dsRNA-dependent line broadening correlates with the previously characterized interactions between dsRBDs and dsRNA. A similar broad-

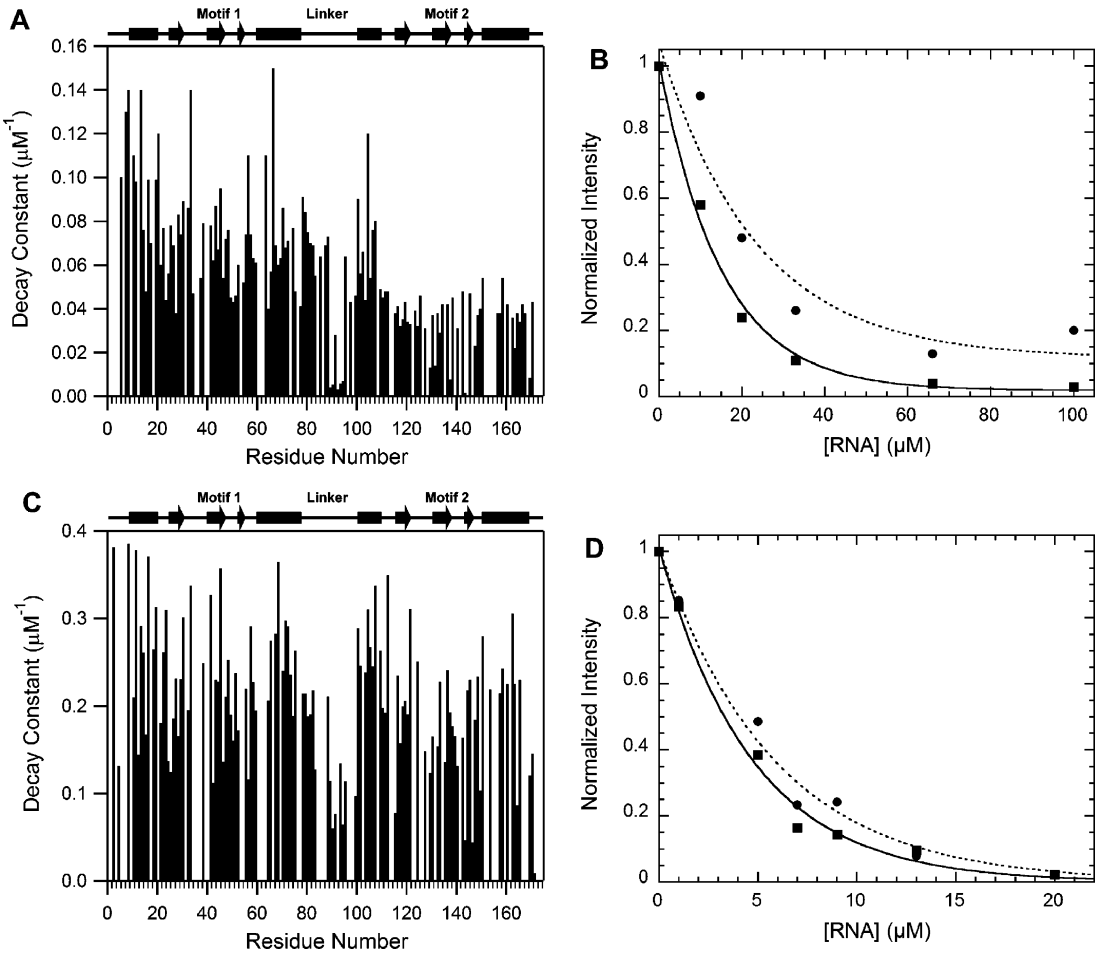

FIGURE 7: Dependence of dsRBD protein NMR signals on dsRNA concentration. (A) Sequence specific constants for NMR signal decays with increasing concentrations of 20-mer dsRNA. (B) Peak intensities averaged over residues within dsRBM1 (■) and dsRBM2 (●) as a function of 20 bp dsRNA concentration. Reciprocal decay constants (1/*k*) were 15.0 ± 1.4 μM for motif 1 and 23.7 ± 8.0 μM for motif 2. (C) Sequence specific exponential decay constants as in panel A except as a function of 40 bp dsRNA concentration. (D) Average intensities as in panel B except with the 40 bp dsRNA. Reciprocal decay constants (1/*k*) were 4.5 ± 0.5 μM for motif 1 and 5.9 ± 8.0 μM for motif 2.

ening pattern is observed for the first motif in dsRBD; however, perturbation of the second motif is limited to helix α1 (Figure 8B).

Binding of dsRBD to the 40 bp RNA also induces broadening; however, the differences in the decay constants between motifs 1 and 2 are much less pronounced (Figure 7C,D). Nevertheless, the regions involved in RNA binding, such as the two α helices, exhibit an enhanced dsRNA-dependent broadening (Figure 8C). These data suggest that the extent of participation of motif 2 in binding RNA is increased with the longer dsRNA sequence. As observed with the 20 bp sequence, the central portion of the linker region remains unperturbed even at the highest concentration of the 40 bp RNA.

DISCUSSION

Our sedimentation velocity and equilibrium data indicate that dsRBD and dsRBM1 exist as homogeneous monomers up to relatively high concentrations. It is well-established that full-length PKR is capable of dimerizing in the absence of RNA (*27*, *28*, *31*, *37*, *40*, *59*, *60*), with a K_d of ~500 μM (*31*). Although it has been reported that dimerization is mediated, at least in part, by interactions involving the dsRNA binding region (*37*, *38*, *40*, *41*), our results suggest that the dimerization interface lies outside this region. Consistent with this interpretation, a complex of the PKR kinase domain with eIF2α crystallizes as a dimer, with the interface primarily involving the N-terminal kinase lobe (*61*). We also do not detect hetero-interaction between the dsRBD and dsRBM1 or between these constructs and full-length PKR. In contrast, interaction between dsRBD and full-length PKR has been reported using affinity chromatography and far-Western assays (*36*, *37*). The origin of these discrepancies is not clear but may reflect the use of affinity tags and indirect assays of protein−protein interactions.

Systematic investigation of the interactions of dsRBD and dsRBM1 with short dsRNA sequences provides new insights into the mechanism of dsRNA binding. The RNA binding stoichiometries measured using sedimentation equilibrium and CD assays agree. However, previous measurements based on gel mobility shift assays have detected lower stoichiometries (*20*, *42*): for example, it was reported that two dsRBDs bind to a 34 bp sequence compared to approximately five that we detect binding to a 35 bp RNA (*42*). Presumably, this difference is associated with dissociation during the electrophoretic separation. We find that the two constructs bind similarly to 15−30 bp sequences, but their behavior diverges with longer RNAs. As expected for

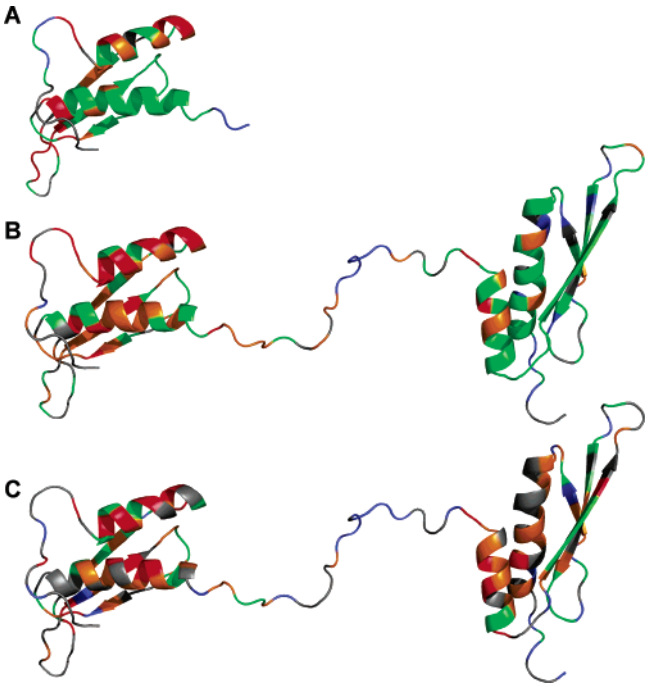

FIGURE 8: Structural mapping of decay constants from Figure 7. (A) Binding of dsRBM1 to 20 bp dsRNA. (B) Binding of dsRBD to 20 bp dsRNA. (C) Binding of dsRBD to 40 bp dsRNA. Residues are colored according to the magnitude of the decay constant (*k*): red, more than one standard deviation (SD) above the mean; orange, mean to one SD above the mean; green, mean to one SD below the mean; and blue, less than one SD below the mean. Residues colored gray are undetermined. The cartoons are based on the first entry in the ensemble of 1QU6 NMR structures for the dsRBD (*11*). The linker between the two domains is disordered in the NMR structure; thus, the relative orientations of the domains and the representation of the linker are arbitrary.

nonspecific dsRNA binding, the binding stoichiometries generally increase with lattice length. For the 15−30 bp sequences, the two constructs are similar, with slightly higher stoichiometries for dsRBM1. For both constructs, the binding stoichiometries are too high to be accommodated by a simple one-dimensional lattice model, and it is necessary to consider overlap of adjacent bound ligands along the helical axis. For dsRBM1, the entire data set fits well to an overlapping ligand model with an *N* of 12 bp and a minimal overlap (Δ) of 4 bp. In the crystal structure of Xlrbpa2 bound to dsRNA (*17*), successive protein ligands pack around the dsRNA at 90° intervals, corresponding to an overlap of 2.75 bp. It is not obvious why Δ is slightly larger than 2.75 for dsRBM1, but it may relate to structural differences between these domains or to the high concentrations used in the crystallographic experiments. Even if we allow for ligand overlap, the site size we determined on the basis of the stoichiometry measurements is somewhat smaller than the ∼16 bp interaction region observed for Xlrbpa2 (*17*) and other dsRBM−RNA complexes (*14*−*16*, *18*, *19*).

It is notable that over the range of 15−30 bp, the stoichiometries for the dsRBD are just slightly higher than those for dsRBM1, indicating that the presence of motif 2 does not double the site size. However, motif 2 strongly enhances the binding affinity for the 20 bp RNA by ∼30-fold, and it has previously been reported that the presence of motif 2 increases the degree of RNA binding (*38*, *62*). These observations can be reconciled by a model in which motif 2 enhances binding affinity but makes only limited

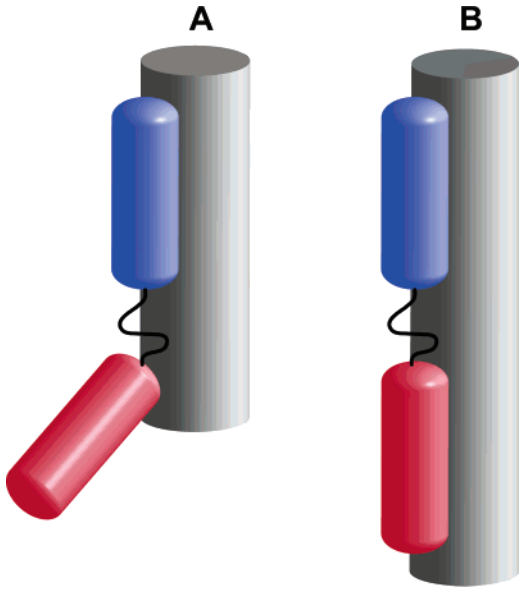

FIGURE 9: Models for the binding modes governing interactions of the dsRBD with short (A) and long (B) dsRNA sequences.

contacts with the dsRNA. Our NMR data show that interactions between dsRBD and the 20 bp RNA occur predominantly on motif 1 with minor contributions from a region other than the N-terminal helix of motif 2. In particular, the portions of motif 1 in dsRBM1 and the dsRBD that are most rapidly broadened in RNA titrations are similar and map to three regions previously implicated in RNA binding: helix α1, the loop between β1 and β2, and the N-terminus of helix α2. In contrast, the most sensitive region of motif 2 is limited to helix α1. These results agree with chemical shift perturbation analysis of the dsRBD−TAR interaction where it was observed that dsRBM2 is less involved in RNA recognition (*13*). Thus, dsRBD likely binds similarly to short linear dsRNAs and TAR, and Figure 9A illustrates this binding mode in which the interaction of dsRBM2 is limited to the N-terminus.

Although the data for the dsRBM1−dsRNA interactions conform to the model predictions for all sequences that we examined, for dsRBD the stoichiometries deviate strongly for longer RNAs and actually decrease between 35 and 40 bp. This decrease in stoichiometry suggests that a different binding mode with a larger site size or larger minimal overlap becomes dominant with longer dsRNA sequences. This new binding mode must confer significantly enhanced binding affinity, since it is stable even at a high molar excess of dsRBD, which would tend to drive the system to adopt the binding model with a higher stoichiometry. NMR shows that the onset of line broadening occurs at lower dsRNA concentrations and that the effects of dsRNA are more evenly distributed between dsRBM1 and dsRBM2 with the longer, 40 bp dsRNA. Taken together, these results point to a model in which dsRBM1 has a dominant role in molecular recognition with short RNA sequences whereas both dsRBM1 and dsRBM2 contribute significantly in binding to longer dsRNA sequences (Figure 9).

What is the functional significance of the two binding modes? It is interesting to note that the deviation from the expected binding stoichiometries occurs around 35 bp, which is close to the minimal length of dsRNA reported to be capable of activating PKR (*29*). Thus, more extensive

interaction of motif 2 with dsRNA may be associated with activation. An analogous correlation was reported on the basis of affinity cleavage experiments. In these studies, RNAs that activate PKR, such as HIV TAR, bind both motifs of the dsRBD, whereas inhibitor viral RNAs, such as adenovirus VAI, bind only dsRBM1 (*48*). Recent NMR shift perturbation measurements dispute these observations and indicate that similar regions of dsRBD interact with viral RNA activators and inhibitors (*58*). Correlation between the RNA binding behavior of the dsRBD and activation of full-length PKR must be interpreted with caution, since the holoenzyme and the dsRBD fragment may interact differently with RNA. Further studies comparing the RNA binding behavior of dsRBD and the full-length enzyme are in progress with the aim of better defining the contribution of different binding modes to enzymatic activation.

ACKNOWLEDGMENT

We thank Arlene Albert for use of the CD instrument and Bill Matousek for help with protein purification during the early stages of this project.

REFERENCES

1. Clemens, M. J., and Elia, A. (1997) The double-stranded RNA-dependent protein kinase PKR: Structure and function, *J. Interferon Cytokine Res. 17*, 503−24.
2. Dever, T. E. (1999) Translation initiation: Adept at adapting, *Trends Biochem. Sci. 24*, 398−403.
3. St. Johnston, D., Brown, N. H., Gall, J. G., and Jantsch, M. (1992) A conserved double-stranded RNA-binding domain, *Proc. Natl. Acad. Sci. U.S.A. 89*, 10979−83.
4. Green, S. R., and Mathews, M. B. (1992) Two RNA-binding motifs in the double-stranded RNA-activated protein kinase, DAI, *Genes Dev. 6*, 2478−90.
5. Saunders, L. R., and Barber, G. N. (2003) The dsRNA binding protein family: Critical roles, diverse cellular functions, *FASEB J. 17*, 961−83.
6. Tian, B., Bevilacqua, P. C., Diegelman-Parente, A., and Mathews, M. B. (2004) The double-stranded RNA binding motif: Interference and much more, *Nat. Rev. Mol. Cell Biol. 5*, 1013−23.
7. Fierro-Monti, I., and Mathews, M. B. (2000) Proteins binding to duplexed RNA: One motif, multiple functions, *Trends Biochem. Sci. 25*, 241−6.
8. Kharrat, A., Macias, M. J., Gibson, T. J., Nilges, M., and Pastore, A. (1995) Structure of the dsRNA binding domain of *E. coli* RNase III, *EMBO J. 14*, 3572−84.
9. Bycroft, M., Grunert, S., Murzin, A. G., Proctor, M., and St. Johnson, D. (1995) NMR solution structure of a dsRNA binding domain from *Drosophila staufen* protein reveals homology to the N-terminal domain of ribosomal protein S5, *EMBO J. 14*, 3563−71.
10. Blaszczyk, J., Tropea, J. E., Bubunenko, M., Routzahn, K. M., Waugh, D. S., Court, D. L., and Ji, X. (2001) Crystallographic and modeling studies of RNase III suggest a mechanism for double-stranded RNA cleavage, *Structure 9*, 1225−36.
11. Nanduri, S., Carpick, B. W., Yang, Y., Williams, B. R., and Qin, J. (1998) Structure of the double-stranded RNA binding domain of the protein kinase PKR reveals the molecular basis of its dsRNA-mediated activation, *EMBO J. 17*, 5458−65.
12. Stefl, R., Xu, M., Skrisovska, L., Emeson, R. B., and Allain, F. H. (2006) Structure and specific RNA binding of ADAR2 double-stranded RNA binding motifs, *Structure 14*, 345−55.
13. Kim, I., Liu, C. W., and Puglisi, J. D. (2006) Specific recognition of HIV TAR RNA by the dsRNA binding domains (dsRBD1-dsRBD2) of PKR, *J. Mol. Biol. 358*, 430−42.
14. Wu, H., Henras, A., Chanfreau, G., and Feigon, J. (2004) Structural basis for recognition of the AGNN tetraloop RNA fold by the double-stranded RNA-binding domain of Rnt1p RNase III, *Proc. Natl. Acad. Sci. U.S.A. 101*, 8307−12.
15. Leulliot, N., Quevillon-Cheruel, S., Graille, M., van Tilbeurgh, H., Leeper, T. C., Godin, K. S., Edwards, T. E., Sigurdsson, S. T., Rozenkrants, N., Nagel, R. J., Ares, M., and Varani, G. (2004) A new α-helical extension promotes RNA binding by the dsRBD of Rnt1p RNAse III, *EMBO J. 23*, 2468−77.
16. Blaszczyk, J., Gan, J., Tropea, J. E., Court, D. L., Waugh, D. S., and Ji, X. (2004) Noncatalytic assembly of ribonuclease III with double-stranded RNA, *Structure 12*, 457−66.
17. Ryter, J. M., and Schultz, S. C. (1998) Molecular basis of double-stranded RNA-protein interactions: Structure of a dsRNA-binding domain complexed with dsRNA, *EMBO J. 17*, 7505−13.
18. Ramos, A., Grunert, S., Adams, J., Micklem, D. R., Proctor, M. R., Freund, S., Bycroft, M., St Johnston, D., and Varani, G. (2000) RNA recognition by a Staufen double-stranded RNA-binding domain, *EMBO J. 19*, 997−1009.
19. Gan, J., Tropea, J. E., Austin, B. P., Court, D. L., Waugh, D. S., and Ji, X. (2006) Structural insight into the mechanism of double-stranded RNA processing by ribonuclease III, *Cell 124*, 355−66.
20. Bevilacqua, P. C., and Cech, T. R. (1996) Minor-groove recognition of double-stranded RNA by the double-stranded RNA-binding domain of the RNA-activated protein kinase PKR, *Biochemistry 35*, 9983−94.
21. Liu, Y., Lei, M., and Samuel, C. E. (2000) Chimeric double-stranded RNA-specific adenosine deaminase ADAR1 proteins reveal functional selectivity of double-stranded RNA binding domains from ADAR1 and protein kinase PKR, *Proc. Natl. Acad. Sci. U.S.A. 97*, 12541−6.
22. Nagel, R., and Ares, M., Jr. (2000) Substrate recognition by a eukaryotic RNase III: The double-stranded RNA-binding domain of Rnt1p selectively binds RNA containing a 5′-AGNN-3′ tetraloop, *RNA 6*, 1142−56.
23. Spanggord, R. J., and Beal, P. A. (2001) Selective binding by the RNA binding domain of PKR revealed by affinity cleavage, *Biochemistry 40*, 4272−80.
24. Vattem, K. M., Staschke, K. A., and Wek, R. C. (2001) Mechanism of activation of the double-stranded-RNA-dependent protein kinase, PKR: role of dimerization and cellular localization in the stimulation of PKR phosphorylation of eukaryotic initiation factor-2 (eIF2), *Eur. J. Biochem. 268*, 3674−84.
25. Nanduri, S., Rahman, F., Williams, B. R. G., and Qin, J. (2000) A dynamically tuned double-stranded RNA binding mechanism for the activation of antiviral kinase PKR, *EMBO J. 19*, 5567−74.
26. Wu, S., and Kaufman, R. J. (2004) trans-Autophosphorylation by the isolated kinase domain is not sufficient for dimerization or activation of the dsRNA-activated protein kinase PKR, *Biochemistry 43*, 11027−34.
27. Wu, S., and Kaufman, R. J. (1997) A model for the double-stranded RNA (dsRNA)-dependent dimerization and activation of the dsRNA-activated protein kinase PKR, *J. Biol. Chem. 272*, 1291−6.
28. Carpick, B. W., Graziano, V., Schneider, D., Maitra, R. K., Lee, X., and Williams, B. R. G. (1997) Characterization of the solution complex between the interferon-induced double-stranded RNA-activated protein kinase and HIV-I trans-activating region RNA, *J. Biol. Chem. 272*, 9510−6.
29. Manche, L., Green, S. R., Schmedt, C., and Mathews, M. B. (1992) Interactions between double-stranded RNA regulators and the protein kinase DAI, *Mol. Cell. Biol. 12*, 5238−48.
30. Lemaire, P. A., Tessmer, I., Craig, R., Erie, D. A., and Cole, J. L. (2006) Unactivated PKR exists in an open conformation capable of binding nucleotides, *Biochemistry 45*, 9074−84.
31. Lemaire, P. A., Lary, J., and Cole, J. L. (2005) Mechanism of PKR activation: Dimerization and kinase activation in the absence of double-stranded RNA, *J. Mol. Biol. 345*, 81−90.
32. Kostura, M., and Mathews, M. B. (1989) Purification and activation of the double-stranded RNA-dependent eIF-2 kinase DAI, *Mol. Cell. Biol. 9*, 1576−86.
33. Hovanessian, A. G., and Kerr, I. M. (1979) The (2′-5′) oligoadenylate (pppA2′-5′A2′-5′A) synthetase and protein kinase(s) from interferon-treated cells, *Eur. J. Biochem. 93*, 515−26.
34. Hunter, T., Hunt, T., Jackson, R. J., and Robertson, H. D. (1975) The characteristics of inhibition of protein synthesis by double-stranded ribonucleic acid in reticulocyte lysates, *J. Biol. Chem. 250*, 409−17.
35. Kimchi, A., Zilberstein, A., Schmidt, A., Shulman, L., and Revel, M. (1979) The interferon-induced protein kinase PK-i from mouse L cells, *J. Biol. Chem. 254*, 9846−53.
36. Rende-Fournier, R., Ortega, L. G., George, C. X., and Samuel, C. E. (1997) Interaction of the human protein kinase PKR with the mouse PKR homolog occurs via the N-terminal region of PKR

and does not inactivate autophosphorylation activity of mouse PKR, *Virology 238*, 410−23.
37. Patel, R. C., Stanton, P., McMillan, N. M., Williams, B. R., and Sen, G. C. (1995) The interferon-inducible double-stranded RNA-activated protein kinase self-associates in vitro and in vivo, *Proc. Natl. Acad. Sci. U.S.A. 92*, 8283−7.
38. Tian, B., and Mathews, M. B. (2001) Functional characterization of and cooperation between double-stranded RNA binding motifs of the protein kinase PKR, *J. Biol. Chem. 276*, 9936−44.
39. Tan, S. L., Gale, M. J., Jr., and Katze, M. G. (1998) Double-stranded RNA-independent dimerization of interferon-induced protein kinase PKR and inhibition of dimerization by the cellular P58IPK inhibitor, *Mol. Cell. Biol. 18*, 2431−43.
40. Cosentino, G. P., Venkatesan, S., Serluca, F. C., Green, S. R., Mathews, M. B., and Sonenberg, N. (1995) Double-stranded-RNA-dependent protein kinase and TAR RNA-binding protein form homo- and hetero-dimers in vivo, *Proc. Natl. Acad. Sci. U.S.A. 92*, 9445−9.
41. Wu, S., and Kaufman, R. J. (1996) Double-stranded (ds) RNA binding and not dimerization correlates with the activation of the dsRNA-dependent protein kinase (PKR), *J. Biol. Chem. 271*, 1756−63.
42. Schmedt, C., Green, S. R., Manche, L., Taylor, D. R., Ma, Y., and Mathews, M. B. (1995) Functional characterization of the RNA-binding domain and motif of the double-stranded RNA-dependent protein kinase DAI (PKR), *J. Mol. Biol. 249*, 29−44.
43. Ucci, J. W., and Cole, J. L. (2004) Global analysis of nonspecific protein-nucleic interactions by sedimentation equilibrium, *Biophys. Chem. 108*, 127−40.
44. Minks, M. A., West, D. K., Benvin, S., and Baglioni, C. (1979) Structural requirements of double-stranded RNA for the activation of 2′,5′-Oligo(A) polymerase and protein kinase of interferon-treated HeLa cells, *J. Biol. Chem. 254*, 10180−3.
45. Bevilacqua, P. C., George, C. S., Samuel, C. E., and Cech, T. R. (1998) Binding of the protein kinase PKR to RNAs with secondary structure defects: Role of the tandem A-G mismatch and noncontinguous helices, *Biochemistry 37*, 6303−16.
46. Katze, M. G., DeCorato, D., Safer, B., Galabru, J., and Hovanessian, A. G. (1987) Adenovirus VAI RNA complexes with the 68 000 Mr protein kinase to regulate its autophosphorylation and activity, *EMBO J. 6*, 689−97.
47. Maitra, R., McMillan, N. A. J., Desai, S., McSwiggen, J., Hovanessian, A. G., Sen, G., Williams, B. R. G., and Silverman, R. H. (1994) HIV-1 TAR RNA has an intrinsic ability to activate interferon-inducible enzymes, *Virology 204*, 823−7.
48. Spanggord, R. J., Vuyisich, M., and Beal, P. A. (2002) Identification of binding sites for both dsRBMs of PKR on kinase-activating and kinase-inhibiting RNA ligands, *Biochemistry 41*, 4511−20.
49. Minton, A. P. (1997) Alternative strategies for the characterization of associations in muticomponent solutions via measurements of sedimentation equilibrium, *Prog. Colloid Polym. Sci. 107*, 11−9.
50. Cole, J. L. (2004) Analysis of heterogeneous interactions, *Methods Enzymol. 384*, 212−32.
51. Schuck, P. (2000) Size-distribution analysis of macromolecules by sedimentation velocity ultracentrifugation and Lamm equation modeling, *Biophys. J. 78*, 1606−19.
52. Schuck, P. (1998) Sedimentation analysis of noninteracting and self-associating solutes using numerical solutions to the Lamm equation, *Biophys. J. 75*, 1503−12.
53. Epstein, I. R. (1978) Cooperative and non-cooperative binding of large ligands to a finite one-dimensional lattice: A model for ligand-oligonucleotide interactions, *Biophys. Chem. 8*, 327−39.
54. Latt, S. A., and Sober, H. A. (1967) Protein-nucleic acid interactions. II. Oligopeptide-polyribonucleotide binding studies, *Biochemistry 6*, 3293−306.
55. Munro, P. D., Jackson, C. M., and Winzor, D. J. (2000) Consequences of the non-specific binding of a protein to a linear polymer: Reconciliation of stoichiometric and equilibrium titration data for the thrombin-heparin interaction, *J. Theor. Biol. 203*, 407−18.
56. Nanduri, S., Carpick, B., Yang, Y., Williams, B. R. G., and Qin, J. (1998) ^{1}H, ^{13}C, ^{15}N resonance assignments of the 20 kDa double stranded RNA binding domain of PKR, *J. Biomol. NMR 12*, 349−51.
57. Bloomfield, V. A., Crothers, D. M., and Tinocco, I., Jr. (2000) *Nucleic Acids: Structures, properties, and functions*, Unversity Science Books, Sausalito, CA.
58. McKenna, S. A., Kim, I., Liu, C. W., and Puglisi, J. D. (2006) Uncoupling of RNA binding and PKR kinase activation by viral inhibitor RNAs, *J. Mol. Biol. 358*, 1270−85.
59. Langland, J. O., and Jacobs, B. L. (1992) Cytosolic double-stranded RNA-dependent protein kinase is likely a dimer of partially phosphorylated Mr = 66,000 subunits, *J. Biol. Chem. 267*, 10729−36.
60. Ortega, L. G., McCotter, M. D., Henry, G. L., McCormack, S. J., Thomis, D. C., and Samuel, C. E. (1996) Mechanism of interferon action. Biochemical and genetic evidence for the intermolecular association of the RNA-dependent protein kinase PKR from human cells, *Virology 215*, 31−9.
61. Dar, A. C., Dever, T. E., and Sicheri, F. (2005) Higher-order substrate recognition of eIF2α by the RNA-dependent protein kinase PKR, *Cell 122*, 887−900.
62. Green, S. R., Manche, L., and Mathews, M. B. (1995) Two functionally distinct RNA-binding motifs in the regulatory domain of the protein kinase DAI, *Mol. Cell. Biol. 15*, 358−64.

BI061531O